PCCP

Phonon and magnetoelastic coupling in Al0.5Ga0.5FeO3: Raman, magnetization and neutron diffraction studies

Journal:	*Physical Chemistry Chemical Physics*
Manuscript ID	CP-ART-11-2019-006124.R1
Article Type:	Paper
Date Submitted by the Author:	13-Feb-2020
Complete List of Authors:	Mishra, K; University of Puerto Rico Rio Piedras, physics Shukla, Rakesh; BARC, Chemistry Division; Krishna, P. S. R.; BHABHA ATOMIC RESEARCH CENTRE, Solid State Physics Division Babu, P.D.; UGC-DAE-CSR Consortium, Mumbai, 400085 Achary, S; Bhabha Atomic Research Centre, Mumbai 400 085, India, Chemistry Division Katiyar, Ram; University of Puerto-Rico, Rio-piedras, Physics Scott, James; School of Physics, University of St. Andrews, St. Andrews, United Kingdom KY19 9SS

Phonon and magnetoelastic coupling in $Al_{0.5}Ga_{0.5}FeO_3$: Raman, magnetization and neutron diffraction studies

K. K. Mishra,[a] R. Shukla,[b] P. S. R. Krishna,[c] P. D. Babu,[d] S. N. Achary,[b] R. S. Katiyar,[a] J. F. Scott[a,e]

[a]*Department of Physics and Institute for Functional Nanomaterials, P.O. Box 70377, University of Puerto Rico, San Juan, PR 00936-8377, USA*

[b]*Chemistry Division, Bhabha Atomic Research Centre, Mumbai, 400085*

[c]*Solid State Physics Division, Bhabha Atomic Research Centre, Mumbai, 400085*

[d]*UGC-DAE-CSR Consortium, Mumbai, 400085*

[a,e]*School of Physics, University of St. Andrews, St. Andrews, United Kingdom KY19 9SS*

Abstract

The intriguing coupling phenomena among spin, phonon, and charge degrees of freedom in materials having magnetic, ferroelectric and/or ferroelastic order have been of research interest for the fundamental understanding and technological relevance. We report a detailed study on structure and phonons of $Al_{0.5}Ga_{0.5}FeO_3$ (ALGF), a lead-free magnetoelectric material, carried out using variable temperature dependent powder neutron diffraction and Raman spectroscopy. Neutron diffraction studies suggest that Al^{3+} ions are distributed in one tetrahedrally (BO_4) and three octahedrally (BO_6) coordinated sites of the orthorhombic ($Pc2_1n$) structure and there is no structural transition in the temperature range of 7-800 K. Temperature dependent field-cooled and zero-field-cooled magnetization studies indicate ferrimagnetic ordering below 225 K (T_N), and that is reflected in the low temperature powder neutron diffraction data. An antiferromagnetic type arrangement of Fe^{3+} ions with net magnetic moment of 0.13 μ_B/Fe^{3+} was observed from powder neutron diffraction analysis and it corroborates the findings from magnetization studies. At the magnetic transition temperature, no drastic change in lattice strain was observed, while significant changes in phonons were observed in the Raman spectra. The deviation of several mode frequencies from the standard anharmonicity model in the ferrimagnetic phase (below 240 K) is attributed to coupling effect between spin and phonon. Spin-phonon coupling effect is discernable from Raman bands located at 270, 425, 582, 695, 738, and 841 cm^{-1}. Their coupling strengths (λ) have been estimated using our phonon spectra and magnetization results. BO_n (n = 4, 6) libration (restricted rotation) mode at 270 cm^{-1} has the largest coupling constant ($\lambda \sim 2.3$), while the stretching vibrations located at 695 and 738 cm^{-1} have the lowest coupling constant ($\lambda \sim 0.5$). In addition to the libration mode, several internal stretching and bending modes of polyhedral units are strongly affected by spin ordering.

INTRODUCTION

Magnetoelectric and multiferroic materials are materials that exhibit coupling of more than one ferroic ordering such as ferro/ferri-magnetic, ferroelectric, and elastic order.[1,4] Such materials have attracted significant attention of the research community to understand the coupling among spin, phonon, and polarization order parameters. The coupled ferroic ordering makes them potential materials for applications in multifunctional devices like spintronics, data storage, microelectronics devices etc.[5-15] However, the technology is still limited due to non-availability of materials with multiferroicity near ambient temperature and/or weak coupling of the order parameters. Till date only a few magnetoelectric multiferroic materials like $BiFeO_3$, $TbMnO_3$, $Pb(Fe_{0.5}Nb_{0.5})O_3$, $AlFeO_3$, and $GaFeO_3$ are known to exhibit magnetoelectric coupling near ambient temperature.[16-21,22] In last decade, extensive research efforts have been devoted to magnetoelectric multiferroic $BiFeO_3$ (ferroelectric transition temperature T_c ~1143 K and antiferromagnetic Neel temperature T_N ~643 K) to understand the origin and ordering of ferroic order parameters.[1,2,23] Similarly, magnetoelectric properties of $GaFeO_3$ and $AlFeO_3$ have also been explored in several studies. Ferrimagnetic ordering in bulk $GaFeO_3$ was observed around 210 K while that in thin films was noticed near 300 K.[22] At ambient temperature, very high polarization (~ 35 μC cm^{-2}) and a large coercive field (±1400 kV cm^{-1}) have been reported in $GaFeO_3$ thin films, and they are attributed to the geometry of octahedral units in the structure.[22] However, the understanding of spin-phonon coupling and spin dynamics in such materials is still limited.

Study of phonons and their coupling with spin degree of freedom is important for understanding of the fundamental origin of multiferroicity and its thermodynamic properties. Often structural and magnetic orderings are manifested in their phonons, and thus the behavior of phonons with temperature, and/or pressure can facilitate understanding of the magnetoelectric effects in multiferroics.[24-29] The change in phonon mode frequencies of magnetoelectric material as a function of temperature at ambient pressure occurs due to lattice anharmonicity and spin-phonon coupling. The lattice anharmonicity arises from chemical interactions, i.e. bonding among various atoms, while the spin-phonon coupling arises from the interactions of magnetic ions in the magnetically ordered lattice.[28-29] In general, spin-phonon coupling plays an important role in dictating several exotic properties such as magneto-ferroelectricity, magnetoelectricity, and hence, it guides to tune structural properties by applied external magnetic field. Raman spectroscopy is known to be sensitive to structural changes and phonon renormalization induced by spin exchange integral[30,31,32]; it can shed light on the possible coupling among the different ferroic order parameters in

multiferroics. The lattice anharmonicity and spin-phonon coupling components can be decoupled by investigating Raman spectra as a function of temperature in a magnetoelectric material.

Recently, a number of studies on structural and magnetic properties of magnetoelectric $GaFeO_3$ and $AlFeO_3$ have been reported in literature.[21,33,34,35] These materials are isostructural and exhibit ferrimagnetic transitions near ambient temperature (T_N for $GaFeO_3$ and $AlFeO_3$ are 210 and 250 K, respectively). However, the experimental results on spin-phonons coupling are reported only in a few reports.[21,31] The presence of spin-phonon coupling in $GaFeO_3$ has been observed from the temperature evolution of mode frequency of 374 cm^{-1} phonon associated with oxygen polyhedra.[33] Similarly, spectroscopic studies on $AlFeO_3$[21] indicate a strong phonon frequency modulation as well as coupling between second order phonon and two magnon excitation below the magnetic ordering temperature (T_N). The intermediate composition of these two, $Al_{0.5}Ga_{0.5}FeO_3$ (ALGF) also belongs to the class of near room temperature magnetoelectric compounds, and has an orthorhombic structure with eight formula units per unit cell.[33] The cations occupy four crystallographically distinct sites, and they can be grouped into two different symmetries, viz., one tetrahedrally coordinated site and three octahedrally coordinated sites. In these compounds, two of the octahedra are highly distorted, while the tetrahedron is almost regular. Further, in these solid solution compositions, the degree of distortion is related to cation disorder and ionic radii of the cations. The electric polarization in such structures originates from the distortions of the two octahedral sites.[21,23,33] Thus, the fundamental understanding of the couplings of spin-phonon of such materials is expected to be useful for designing of appropriate chemical composition and structure to improve magnetoelastic and magnetoelectric properties. Furthermore, as in other magnetoelectrics[11], the present ALGF material can be quite useful for development of green solid-state cooling technologies. Interestingly, formation of new polymorphs can be obtained in ALGF under high pressure facilitated by magnetic interaction in contrast to other similar non-magnetic oxides.[28-29]

In this manuscript, the details of temperature dependent structural and vibrational properties of $Al_{0.5}Ga_{0.5}FeO_3$ in ferrimagnetic and paramagnetic phase (7-800 K) are reported. Polycrystalline samples of ALGF were prepared by high temperature solid state reaction method and investigated by variable temperature Raman spectroscopic, neutron diffraction, and magnetization studies. From the temperature dependent unit cell parameters and phonon modes, spin modulated phonons and their spin-phonon coupling have been deduced. The behavior of phonon modes with temperature was analyzed using the standard phonon anharmonicity model to decouple the spin-phonon coupling effect. In combination with Heisenberg's exchange (spin-spin) correlation function $\langle S_i.S_j \rangle$, the spin-phonon coupling strengths (λ) have been evaluated. The renormalization of phonon mode frequencies induced by spin exchange integral

was evident for ALGF. Librational, and several other internal stretching and bending modes involving the polyhedral units were found to be strongly affected by magnetic ordering.

EXPERIMENTAL DETAILS

Polycrystalline samples of ALGF were prepared by solid-state reaction method using Ga_2O_3, Fe_2O_3 and Al_2O_3 (all with purity 99.99%, Alfa Aesar) as starting materials. Stoichiometric amounts of the reactants were mixed by high-energy ball milling (Pulverisette Fritsch Planetary mill, model P7) at 600 rpm for 14 h in isopropyl alcohol. The slurry was dried at ambient conditions. The dried powder was again mixed using an agate mortar and pestle, and then calcined at 1573 K for 10 h in air using a Carbolite HTF1700 furnace. A homogeneous mixture of the calcined powder and polyvinyl alcohol (by 7 wt %) was prepared by grinding them together in an agate mortar. Cylindrical pellets (diameter of 13 mm and height of 2-3 mm) of this mixture were prepared by pressurizing with an uniaxial pressure of 6 tons. These pellets were sintered at 1663 K for 5 h in air. The heating and cooling rates for the calcination and sintering processes were 2 K/min. Surface morphology and microstructure (i.e., grain size, grain distribution, voids, etc.) of the samples were studied using a scanning electron microscope (SEM) (JEOL JSM-6480LV) at a magnification of 2000X operated at an accelerating voltage of 20 kV. Elemental analyses were carried out by energy-dispersive x-ray (EDX) analyses using EDX Genesis 2000 attachment on the same SEM. The composition and chemical states of iron in the sample were confirmed by high-resolution x-ray photoemission spectroscopy (XPS). Initially, single-phase of ALGF was confirmed from the x-ray diffraction (XRD) results at room temperature. The XRD data were recorded using Cu-Kα radiation, employing a Smartlab x-ray diffractometer operated in the Bragg-Brentano (θ–2θ) geometry at 40 kV and 40 mA. Subsequently, detailed structural characterizations were carried out by using powder neutron diffraction (PND) technique. The PND data below ambient temperature were collected from a vanadium metal sample holder filled with finely powdered sample. Temperature was controlled by a closed cycle refrigerator-based cryostat. Neutron diffraction data above room temperature were collected using a thin fused quartz tube filled with the powdered sample. These temperature dependent PND patterns were recorded using an array of five sensitive detectors on a Debye Scherrer type powder neutron diffractometer at Dhruva research reactor, Trombay, India.[36] PND data at low temperature were collected in heating mode, after equilibrating at 7 K for about 6 h. Above room temperature, the sample was heated to 773 K and the data were collected in cooling cycle. At each temperature the sample was equilibrated for 1 h to collect the diffraction data over a period of 8 h. Rietveld refinement of the PND patterns were carried out using the FullProf Suite software.[37] Raman spectra of ALGF were recorded using a HORIBA Jobin Yvon micro-Raman spectrometer (model:

T64000) equipped with an Olympus microscope and a 50× long-working distance objective. The measurements were carried out in back scattering geometry employing 514.5 nm line of an Ar-ion laser as excitation source. The scattered signal was analyzed using a triple monochromator and detected by a CCD detector. The spectrometer resolution for 1800 l/mm grating was ~1 cm^{-1}. Temperature dependent Raman spectra measurements were carried out using a Linkam heating and cooling stage ensuring a temperature stability of ± 0.1 K. To obtain a good signal-to-noise ratio the laser power and data acquisition time were optimized. The spectra were analyzed employing damped harmonic oscillator model to obtain the spectral parameters such as Raman band position, linewidth, and band intensity. Temperature and field dependent magnetization studies were carried out using a PPMS DynaCool (Quantum design) operated in VSM module. Field cooled (FC) and zero field cooled (ZFC) magnetization traces were measured from 3 to 375 K in an applied field of 1000 Oe. *M-H* loops were recorded at several temperatures up to a maximum field of ±9 T.

RESULTS AND DISCUSSION

The morphology and composition of sintered ALGF samples were studied by scanning electron microscopy (SEM) and EDX using gold coated sintered pellet. A typical SEM image and EDX spectrum measured from a fractured surface of the pellet are given in the supplementary data. The scanning electron micrographs of the sintered sample indicated well connected granular structure with average grain size of 3-6 μm, which are uniformly distributed on the surface (**Fig. S1**). X-ray mapping for the constituent elements over the sample surface indicates (**Fig. S1)**) a homogeneous distribution of elements without any segregation or clustering. Nearly stochiometric compositions of the sample are evident from the EDX analysis. Further diffraction studies were carried out on uniform powder obtained after crushing the pellets. Rietveld refinement of the ambient temperature neutron diffraction data was carried out to obtain the structure of ALGF. Structural parameters of $GaFeO_3$ reported earlier in literature[33] were taken as the initial model parameters for the refinement. In the ideal $GaFeO_3$ structure, Ga occupies one tetrahedral (M1) and one octahedral (M2) site, while Fe occupies two octahedral (M3 and M4) sites. In the model structure of ALGF, the tetrahedral and octahedral sites of Ga were considered for Ga and Al, each with 0.5 occupancy. The background of the diffraction pattern was modeled by a linear interpolation of selected points to generate a smoothly varying background profile, and the Bragg peaks were fitted using pseudo-Voigt profile functions. Initially the scale, unit cell parameters and half-width parameters for peak profiles were refined to obtain appropriate profile matching. Subsequently, the position coordinates and isotropic thermal parameters for the individual atoms were refined. The occupation numbers of cations at different sites were finally refined with a constraint of maximum occupancy for each site as 1. Atomic isotropic displacement parameters (B $(Å)^2 = 8\pi^2U$) were used in the refinements.[38-39] The final Rietveld refinement plot for ALGF at room

temperature is shown in **Fig. 1a**. The refined structural parameters and typical interatomic distances in ALGF are given in **Table 1 and 2**, respectively. Since the thermal neutron scattering lengths for the elements are appreciably distinct (O: 5.803 fm; Ga: 7.288 fm, Al: 3.449 fm, and Fe: 9.450 fm), it facilitates accurate determination of the atomic positions and occupancies. As mentioned earlier, the crystal structure of ALGF has four different cation sites, named as M1, M2, M3 and M4, and six sites for O^{2-} ions. All cation sites except M1 are octahedrally coordinated and the M1 site is tetrahedrally coordinated with O^{2-} ions. From the refined structural parameters, it is observed that all these cation sites are occupied by Al^{3+}, Fe^{3+}, and Ga^{3+} ions. The distribution of these cations suggests that the majority of Al^{3+} ions occupy the tetrahedral M1 and octahedral M2 sites; Al^{3+} and Ga^{3+} ions partially occupy the M3 and M4 sites, which are mainly Fe sites of $AlFeO_3$ and $GaFeO_3$. [33,40,41] It is observed that about 21% of Fe^{3+} ions are at the Ga sites (M1 and M2), and the M3 and M4 sites are occupied by 12% and 14% of Al^{3+} ions, respectively. The distribution of cations can be related to their similar oxidation states and also similar preferences for tetrahedral and octahedral sites; and such distribution of cations appears as diffusive in the magnetic properties as explained in a later section. The octahedral $M1O_6$, $M2O_6$ and $M3O_6$ units are linked by sharing their edges, while the tetrahedral $M1O_4$ units are linked by sharing corner oxygen atoms. Typical three-dimensional structure of ALGF (**Fig. 1b)** has a double hexagonally close packed oxygen sublattice, where three of the cations (M2, M3 and M4) are at octahedral interstices and one (M1) at tetrahedral interstices.[41] Thus, the structure can be explained as sheets of octahedral units formed by $M2O_6$ and $M4O_6$ units, and they are sandwiched between the layers of octahedral $M3O_6$ and tetrahedral $M1O_4$ units. These layers are connected by sharing the edges of the octahedral units. The typical PND patterns from 7 K to 773 K are shown in **Fig. 2**. It is seen that the patterns recorded at non-ambient temperatures are quite similar to that at room temperature (300 K). However, noticeable differences in intensity of some reflection peaks were observed at low temperatures, and their intensities progressively increase with decreasing temperature. Prominent intensity variation can be noticed in the (110) and (020) reflection peaks located at $2\theta \sim 11.2^{o}$, and 15.3^{o}, respectively (marked by arrows in **Fig. 2**), which are arisen from the magnetic ordering in ALGF lattice.[21] Also, the position of peaks shows noticeable shift towards lower or higher 2θ angles due to temperature induced expansion or contraction of the unit cell. All PND data could be successfully fitted to the orthorhombic ($Pc2_1n$) lattice. For refinement of the temperature dependent PND data, the background points used for the refinement of the ambient temperature neutron diffraction data were considered, and the peak shape parameters of the pseudo-Voigt functions were refined. The occupancies of atoms were kept fixed as obtained from the ambient temperature data. The typical fitted plots for the data recorded at 7 K and 773 K are shown in **Fig. 3**. The intensities of the magnetic peaks could be accounted by the magnetic unit cell with magnetic moments (μ_B) of -3.8, +4.6, -3.8, and +4.4 at M1, M2, M3, and M4 sites, respectively (**Fig. 4)**. The refinements were carried out using the site occupancies as observed at 300 K. The refined position

coordinates of ALGF are given in **Table 3**. These magnetic moments were found to align along the c-axis as reported in $Ga_{2-x}Fe_xO_3$.[20,31] A quantitative analysis of the intensity of the magnetic reflection peaks is useful to determine the evolution of the magnetic phase with temperature.[23,33,42,43] Hence, the normalized integrated intensities of (110) and (020) peaks, essentially arising from the magnetic unit cell of ALGF, are shown in **Fig. 5**. It can be noticed that the intensity of these peaks increases sharply below 225 K, suggesting that the establishment of magnetic ordering is below 225 K, in agreement with the ferrimagnetic Neel temperature (225 K) obtained from our magnetization studies (explained later in this paper) and is close to that reported in the literature.[33] Thus, it can be concluded that ALGF undergoes a paramagnetic to ferrimagnetic phase transition below 225 K and retaining the ambient non-centrosymmetric structure. Further the structural stability of ALGF is concluded from the variation of unit cell parameters with temperature. From the evolution of unit cell parameters with temperature (**Fig. 6)** it can be noticed that the unit cell parameters decrease at a faster rate from 773 to 250 K, and decrease slowly below 250 K. A small but noticeable deviation near T_N could be attributed to the magnetic transition. This deviation is clearly reflected in the variation of unit cell parameters (strain) with temperature. Despite this deviation, the temperature dependence of unit cell parameters can be fitted to a second order polynomial relation (**Fig. S2)**. The smooth variation of the unit cell parameters with only feeble discontinuities near the magnetic transition points to the structural stability of ALGF in the entire temperature range. The average thermal expansion coefficients (α_x (K^{-1}) = $(X_{773}-X_7)/(X_7(773-7))$, where X_{773} and X_7 are the lattice parameter X at 773 K and 7 K, respectively, X = a, b, c) estimated from the obtained unit cell parameters at 7 K and 773 K are: $\alpha_a = 6.198(3) \times 10^{-6}$ K^{-1}, $\alpha_b = 6.791(2) \times 10^{-6}$ K^{-1}, $\alpha_c = 7.053(1) \times 10^{-6}$ K^{-1}, and $\alpha_V = 20.14(3) \times 10^{-6}$ K^{-1}. The ratio of coefficients of axial thermal expansion $\alpha_a:\alpha_b:\alpha_c$ is 1 : 1.10 : 1.13. Thus, the structure has nearly isotropic thermal expansion with a marginally smaller expansion along the a-axis compared to the other two crystal axes. The flexibility of the a-axis is related to the linking of the $M1O_4$ tetrahedra and $M3O_6$ octahedra along the other two directions. In the structure of ALGF, the $M1O_4$ tetrahedra and $M3O_6$ octahedra are linked only at the corner, and thus, it forms a less densely packed layer to mask the expansion along the a- direction.

To study the magnetic ordering in ALGF, FC and ZFC magnetization measurements were carried out in the temperature range 3 to 375 K in an applied field of 1 kOe. Typical FC and ZFC magnetization traces as a function of temperature are shown in **Fig. 7a**. It can be observed that as the temperature is reduced, both magnetization values increase smoothly down to 225 K and sharply increase below this temperature. Also, the FC and ZFC traces are found to be separated at lower temperatures as expected in a ferrimagnetic sample. The separation of these traces indicates that the magnetization depends on the cooling history of the sample and the observed bifurcation of ZFC and FC curves is ascribed to magnetic domain-

walls pinning.[44] As a manifestation of changes in magnetic ordering, one can notice a rapid change in ZFC magnetization curve around 225 K. In addition, the temperature derivative of the ZFC magnetization curve exhibits a minimum around 225 (± 5) K, the ferrimagnetic phase transition temperature T_N. The observed magnetic moment per Fe^{3+} ion is found to be 0.25(2) μ_B at the lowest temperature (3 K), which is reasonably close to that observed from our PND data at 7 K (0.16(3) μB). This difference in magnetic moment values obtained from PND and magnetization measurements is expected due to dependency of PND data analysis on counting statistics of data and least square fitting errors. The magnetic ordering temperature of ALGF is found to be higher than that in $GaFeO_3$[20] but lower compared to $AlFeO_3$.[33] It can be mentioned that a systematic decrease of unit cell parameters of $Ga_{1-x}Al_xFeO_3$ upon substitution of Al^{3+} cations is possible, and hence, it reduces the distance between two nearest Fe^{3+} ions, which in turn favors stronger interaction of Fe^{3+} ions. **Figure 7b** shows the hysteresis loops (*M~H* curves) measured at different temperatures. The *M~H* curves show a discernible hysteresis loop at 3 K with a remanent magnetization M_R of 7.25 emu-gm^{-1} and a coercive field H_c of 3474 Oe, comparable with values reported in similar systems.[33,20] The magnitude of magnetization increases with increasing applied field up to 2.5 T, and it saturates at higher fields (> 2.5 T). Upon increasing temperature, M_R and H_c values were found to monotonically decrease (**inset Fig. 7b**). Significant reduction in these values (at 300 K, M_R ~ 0.44 emu-gm^{-1} and H_c ~ 87 Oe) suggests paramagnetic behavior of ALGF at room temperature and above. Retention of the magnetization at high temperature can be attributed to the existence of magnetically ordered clusters dispersed in the paramagnetic host, as reported in other perovskite solid solutions.[45] We employed XPS study to determine the oxidation state of iron in ALGF and hence, the magnitude of the spin-orbit coupling of iron in ALGF is not emphasized. The oxidation state of iron was studied from X-ray photo electron spectroscopy for the Fe2P edge (**Fig. S3)**. Due to spin-orbit coupling, a doublet corresponding to $Fe2P_{3/2}$ and $Fe2P_{1/2}$ states was observed at binding energies of 714.01 eV and 727.08 eV, respectively. Employing Casa XPS software, the observed asymmetric doublet was deconvoluted using a Shirley background. The presence of Fe^{2+} and Fe^{3+} cations was ascertained from the deconvoluted peaks. The ratio of integrated intensities of the peaks corresponding to Fe^{3+} and Fe^{2+} suggests the presence of a minor fraction of Fe^{2+} in the studied sample. The larger fraction of Fe^{3+}cations in ALGF is concomitant with the observed magnetic behavior of the sample (discussed earlier). It can be mentioned here that the thermodynamic stability of Fe^{3+} and Fe^{2+} cations is comparable, and hence, the presence of Fe^{2+} cation is often encountered in the Fe-based oxides.[46,47]

Since the magnetic transition and magnetoelectric/multiferroic properties are related to the interaction of the magnetic ion (Fe^{3+}) and strains in the lattice, i.e. spin-phonon interaction, further characterizations were carried out by temperature dependent Raman spectroscopic studies. As the primitive orthorhombic unit cell (S. G. *$Pc2_1n$)* of ALGF has 40 atoms (4 M1, 4M2, 4M3, 4M4 and 24 Oxygen), a

total of 120 vibrational degrees of freedom are expected and they are manifested as optical and acoustic modes at the Brillouin zone center (q = 0). For each atomic site, the irreducible representation was obtained from factor group analysis using Halford-Hornig site-group method,[48] as presented in **Table 4**. The total irreducible representation for the optical phonons is $\Gamma_{opt} = 29A_1+30A_2+29B_1+29B_2$ and that for the acoustic phonons is $\Gamma_{acoustic} = A_1+B_1+B_2$. All 117 optical phonons are Raman active. Since the inversion symmetry is absent in the point group C_{2v}, 87 optical phonons ($29A_1 + 29B_1 + 29B_2$) are also infrared active. Raman spectra measured at ambient temperature covering the frequency range 200 to 1900 cm^{-1} is shown in **Fig. 8**. Fourteen Raman active bands were obtained from spectral analysis using Lorentzian functions. The experimental Raman spectrum and its total Lorentzian least square fits along with individual Raman bands are shown in **Fig. 8**. The smaller number of experimental Raman bands as compared to that expected theoretically could be due to insufficient intensity arising from the small polarizability of several phonon modes[49] or accidental degeneracy of several phonon modes. Raman bands below 200 cm^{-1} are not considered in the present study, and this could also account for some of the missing modes. As in other perovskites,[21,49,50] the Raman bands observed below 1000 cm^{-1} correspond to first order phonon scattering process. The high frequency Raman bands above 1000 cm^{-1} are associated with second order phonon and magnon scattering processes. These mode frequencies are presented in **Table 5** along with their assignments carried out in comparison with an earlier report.[51] The librational mode vibrations involving the tetrahedral and octahedral polyhedral units are observed in the frequency range 200-400 cm^{-1}. All polyhedral bending modes are observed between 400 and 500 cm^{-1}. The high frequency polyhedral stretching modes are in the frequency range 500-1000 cm^{-1}. The symmetric stretching vibration involving the tightly bound $M1O_4$ tetrahedra occur in the range 650-1000 cm^{-1}, and those due to the loosely bound $M3O_6$ octahedra unit are observed between 500 and 650 cm^{-1}. To study the effects of changes in the magnetic ordering on phonons, reduced Raman spectra are required. To obtain the reduced Raman spectra, the measured Raman spectra were corrected for the thermal population factor using the expression given below,

$$I_{red\ (\omega)} = \frac{I_{exp(\omega)}}{[n(\omega,T)+1]},$$

where $I_{exp(\omega)}$ is the experimental Raman intensity of the Raman bands and $n(\omega, T) = [\exp(\hbar\omega/k_BT) - 1]^{-1}$ is the Bose-Einstein occupation factor; $\hbar$ and k_B are the Planck and Boltzmann constants, respectively. The reduced Raman spectra measured in the temperature range of 82-400 K are shown in **Fig. 9**. Raman bands of ALGF are found to soften and broaden with increasing temperature. In addition, their intensities are found to reduce. The softening of bands is due to thermal expansion of bonds while the broadening of the linewidth is expected from multi-phonon scattering processes. Raman bands are usually narrower at lower temperature due to larger lifetime of phonon and hence one can expect a better resolution to resolve broad

features. Thus, the analysis of Raman spectra was carried out from the spectrum measured at the lowest temperature i.e. 82 K. The spectrum was analyzed using multi-Lorentzian curve fitting procedure [50] with a suitable background (**Figs. 9 and 10**). The fitting yields fifteen Raman bands (**Table 5**). The fitted parameters obtained for the spectrum at 82 K were used for the analysis of the spectrum recorded at the next temperature. Since there is no splitting or disappearance of the first order Raman bands in the entire temperature range, it indicates structural stability that was also inferred from the temperature dependent neutron diffraction studies. Temperature dependent high frequency Raman spectra in the frequency range 1000-1900 cm^{-1} represent second order two-phonon Raman bands[21] and are likely to have large contributions from the phonon density of states. Apart from zone center, the flat regions of Brillouin zone and other high symmetry k-points have large contribution to the phonon density of states.[52] Therefore, often the phonons that appear in second order process are not exactly double of first order phonon frequency. Raman spectrum at 82 K could be deconvoluted using four Lorentzian functions (**Fig. 10a**)**.** The deconvoluted Raman spectra suggest that the scattering processes have involvement of four second order Raman bands centered at 1271, 1452, 1566 and 1679 cm^{-1}. The band at 1452 cm^{-1} is an overtone of 738 cm^{-1}; 1566 cm^{-1} band can be assigned as a combination of 738 and 841 cm^{-1} stretching modes, and the one at 1679 cm^{-1} corresponds to an overtone of the 841 cm^{-1} band. The weak band at 1271 cm^{-1} is attributed to a two-magnon band which vanishes above the magnetic ordering temperature T_N, as reported in $AlFeO_3$.[21] The temperature dependencies of these mode frequencies are shown in **Fig. 10b**. As expected, the two-magnon mode is hardens and loses intensity with increasing temperature, and disappears above T_N. Under the assumption of spin deviation on adjacent sites, the nearest-neighbor exchange coupling parameter J can be estimated using a two-magnon band energy ω_o using a known expression[21], $\omega_o = J\times(2\times S\times Z\text{-}1)$, where ω_o is two-magnon band energy, S represents spin at the magnetic site (here Fe^{3+} and S = 5/2) and Z corresponds to the number of the nearest neighbour to Fe^{3+} magnetic site (Z = 6). Using the observed two-magnon band energy ω_o = 1271 cm^{-1} (at 82 K), one can estimates J = 5.43 meV, a value close to that obtained by *ab-initio* calculations for $AlFeO_3$ (~6 meV).[21] This further confirms that the 1271 cm^{-1} band is a two-magnon band. Near the magnetic transition temperature T_N, change in slopes for these mode frequencies (except ~1271 cm^{-1}) is noticed, which can be attributed to the coupling between second order phonon and spin ordering as reported in other systems.[24,53]

As mentioned earlier, the change in mode frequency with temperature can have contributions from lattice anharmonicity, quasi-harmonicity, electron-phonon coupling, and spin-phonon coupling effects due to modulation of exchange integral by phonons. Thus, the temperature dependent mode frequencies $\omega(T)$ can be expressed by the following relation,

$$\omega(T) = \omega_o + \Delta\omega(T)_{qh} + \Delta\omega(T)_{anh} + \Delta\omega(T)_{el-ph} + \Delta\omega(T)_{spin-ph},$$

where ω_o is the phonon frequency at absolute zero temperature, $\Delta\omega_{qh}$ represents the quasiharmonic contribution (implicit contribution), $\Delta\omega_{anh}$ corresponds to the contribution from phonon-phonon interaction, $\Delta\omega_{el\text{-}ph}$ and $\Delta\omega_{spin\text{-}ph}$ are the electron-phonon and the spin-phonon coupling effects. Since ALGF is a dielectric, the contribution from electron-phonon coupling effect for the shift in mode frequency $\Delta\omega$ is insignificant and hence can be neglected. Furthermore, the quasiharmonic contribution is expected only when there is a change in interatomic separation brought out by volume change and is related as $\Delta\omega_{anh} \sim \Delta V/V$.[54] From our neutron diffraction studies, the change in unit cell volume, between 7 to 373 K is found to be only about 0.5 % (**Fig. 6**), and hence its contribution to the shift in mode frequency can also be neglected. Therefore, in ALGF only the anharmonic (explicit) and spin-phonon contributions for the observed $\omega(T)$ need to be considered. The ferrimagnetic ordering is realized below T_N only. Therefore, in the high temperature paramagnetic phase, i.e. above T_N, only anharmonicity related to changes in vibrational amplitude at fixed interatomic distance is expected to contribute to the shift in mode frequency.[54] As a consequence of the anharmonicity, phonons exhibit finite lifetime, and decay into two, three or even more phonons.[52] The cubic anharmonicity leads to the decay of a phonon of frequency ω at temperature T into two longitudinal acoustic (LA) phonons each of frequency $\omega_o/2$. This process contributes to Raman mode frequency ω by ω_C as per the relation given below

$$\omega_C = \omega_o + A\left[1 + \frac{2}{exp\left(\frac{\hbar\omega_o}{2k_B T}\right)-1}\right],$$

where A is the coefficient of cubic anharmonicity. Similarly, the quartic anharmonicity of the mode leads to the decay of a phonon of frequency ω into three LA phonons each of frequency $\omega_o/3$ resulting in the change in mode frequency ω by ω_q as

$$\omega_q = \omega_o + B\left[1 + \frac{3}{exp\left(\frac{\hbar\omega_o}{3k_B T}\right)-1} + \frac{3}{\left(exp\left(\frac{\hbar\omega o}{3k_B T}\right)-1\right)^2}\right],$$

where B is the coefficient of quartic anharmonicity.

Therefore, the total contribution to the observed shift in mode frequency $\omega(T)$ in the paramagnetic phase ($> T_N$) can be considered from the cubic and quartic anharmonicity and hence, can be expressed as $\omega = \omega_o + \omega_C + \omega_q$. In our analysis the Raman band frequencies at 270, 425, 582, 695, 738 and 841 cm^{-1} show anomalous hardening near the magnetic ordering temperature, i.e. $T_N \sim 225$ K. Thus, for the high temperature paramagnetic phase, these frequencies were fitted by considering cubic and quartic anharmonicity terms only. A comparison of fitted parameters (**Fig. 11**) indicates that cubic anharmonicity

dominates over the quartic one, which is expected for the paramagnetic phase. The extrapolation of these fitted curves to the low temperature magnetic phase, i.e. below T_N (shown as dashed lines in **Fig. 11**), suggests the thermal evolution of band frequencies in the absence of magnetic spin ordering effect. Thus, the deviation of observed band frequencies $\Delta\omega$ from the extrapolated values can be attributed to contributions from spin-phonon coupling effect. $\Delta\omega$ are related to spin-spin exchange interaction formalism described by the relation, $\Delta\omega = \lambda\langle S_i.S_j\rangle$,[55,31] where λ corresponds to spin-phonon coupling constant, $\langle S_i.S_j\rangle$ is the spin exchange correlation function, and S_i is the spin of the i^{th} Fe-site. The shift in band frequency $\Delta\omega$ (~6 cm^{-1}) is large for the 270 cm^{-1} librational band suggesting that this band has strong spin-phonon coupling effect. The lowest $\Delta\omega$ value (~1 cm^{-1}) for the 738 cm^{-1} stretching band suggests feeble spin-phonon coupling contribution. In ALGF, since the magnetization easy axis is along the c-axis of the lattice, the magnetic ordering is weakly antiferromagnetic along ab-plane. Therefore, a magnetization interaction chain involving Fe cations is expected along the c-axis. The ensemble average of the magnetization chain under molecular field approximation[56] yields, $\langle S_i.S_j\rangle \sim 2[M(T)/M_S]^2$, where M_S is the saturation magnetization and $M(T)$ is the magnetization as a function of temperature. Following the above spin-spin correlation function, one can define $\Delta\omega = 2\lambda[M(T)/M_S]^2$. Thus, the spin-phonon coupling constant λ can be obtained from the slopes of $\Delta\omega$ versus $[M(T)/M_S]^2$ curves for those Raman bands affected by the magnetic ordering. **Figure 12** shows these Raman bands located at 270, 425, 582, 695, 738 and 841 cm^{-1}, and their coupling constant λ values are given in **Table 5**. One can see that the libration mode (270 cm^{-1}) and internal polyhedral modes (425 and 582 cm^{-1}) have larger λ values (in the range 2.3 to 1.3) compared to other modes. The larger values of λ indicate larger contribution of spin exchange interaction to the phonon frequencies. On the other hand, the high frequency stretching bands (> 600 cm^{-1}) of polyhedra are not strongly affected by spin-phonon coupling and their phonon frequencies are weakly renormalized. These estimated coupling strengths for ALGF are comparable with those reported for antiferromagnetic MnF_2 and FeF_2[57] and canted ferromagnetic $Sr_4Ru_3O_{10}$.[55] The present spin-phonon coupling effect in ALGF provides evidence for the renormalization of phonon frequencies due to spin exchange integral.

CONCLUSIONS

Temperature dependent powder neutron diffraction, Raman spectroscopic and magnetic measurements on $Al_{0.5}Ga_{0.5}FeO_3$ revealed that the orthorhombic ($Pc2_1n$) structure is retained in the entire temperature range from 7 to 773 K, and transition from paramagnetic to ferrimagnetic ordering occurs at around 225 K. No drastic changes in structural parameters were observed, except temperature induced contraction or dilation of unit cell parameters due to compression or expansion of the lattice. A feeble but noticeable deviation in the unit cell parameters was observed near the magnetic transition, while drastic changes in the behavior of several phonon modes were observed near the transition temperature T_N. Renormalization of spin-induced

phonon frequencies was observed below T_N~ 225 K. Magnetoelastic coupling constants λ have been estimated for several phonon modes using Heisenberg's spin exchange correlation function. It is revealed that the MO_n (n = 4, 6) librational mode at 270 cm^{-1} has a large coupling constant (λ = 2.3), and the stretching vibrations located at 695 and 738 cm^{-1} have lower coupling constants (λ ~ 0.5). The present study can be useful to interpret the magnetoelastic, magnetoelectric and multiferroic properties of ALGF and other isostructural compounds.

Acknowledgments:

This work was financially supported by DoD Grant No #AFOSR# FA9550-16-1-0295.

The authors confirm that they have no financial interests in this work.

Correspondence and requests for materials should be addressed to karuna.kara@upr.edu

References

1. M. Fiebig, *J. Phys. D: Appl. Phys.*, **2005**, 38, R123-R152.
2. I. E. Dzyaloshinskii, *Sov. Phys. JETP*, **1959**, 10, 628.
3. D. N. Astrov, *Sov. Phys. JETP*, **1960**, 11, 708.
4. A. J. Freeman and H. Schmid, *Magnetoelectric Interaction Phenomena in Crystals (ed) **1975** Proc. MEIPIC-1 (Seattle, USA, 21-24 May 1973)* (London: Gordon and Breach).
5. J. Wang, J. B. Neaton, H. Zheng, V. Nagarajan, S. B. Ogale, B. Liu, D. Viehland, V. Vaithyanathan, D. G. Schlom, U. V. Waghmare, N. A. Spaldin, K. M. Rabe, M. Wuttig and R. Ramesh, *Science*, **2003**, 299, 1719.
6. M. Fiebig, T. Lottermoser, D.Fröhlich, A. V. Goltsev and R. V. Pisarev, *Nature (London)*, **2002**, 419, 818.
7. Y. Tokura, *Science*, **2006**, 312, 1481.
8. A. Roy, R. Gupta and A. Garg, *Adv. Condens. Matter Phys.*, **2012**, 2012, 926290.
9. M. Gajek, M. Bibes, S. Fusil, K. Bouzehouane, J. Fontcuberta, A. Barthélémy and A. Fert, *Nat. Mater.*, **2007**, 6, 296.
10. Duncan H. Moseley, Shelby E. Stavretis, Komalavalli Thirunavukkuarasu, Mykhaylo Ozerov, Yongqiang Cheng, Luke L. Daemen, Jonathan Ludwig, Zhengguang Lu, Dmitry Smirnov, Craig M. Brown, Anup Pandey, A.J. Ramirez-Cuesta, Adam C. Lamb, Mihail Atanasov, Eckhard Bill, Frank Neese & Zi-Ling Xue, *Nat. Commun.*, **2018**, 9, 2572.
11. Arun K. Sagotra, Daniel Errandonea & Claudio Cazorla, *Nat. Commun.*, **2017**, 8, 963.
12. R. Ramesh & Nicola A. Spaldin, *Nat. Mater.*, **2007**, 6, 21.
13. S.-W. Cheong & M. Mostovoy, *Nat. Mater*., **2007**, 6, 13.
14. A. Lunghi, F. Totti, S. Sanvito & R. Sessoli, *Chem. Sci.*, **2017**, **8**, 6051.
15. C. Chiorescu, J. J. Neumeier & J. L. Cohn, *Phys Rev Lett.*, **2008**, 101, 257202.
16. T. Zhao, A. Scholl, F. Zavaliche, K. Lee, M. Barry, A. Doran, M. P. Cruz, H.Y.Chu, C. Ederer, N. A. Spaldin, R. R. Das, D. M. Kim, S. H. Baek, C. B. Eom and R. Ramesh, *Nat. Mater*., **2006**, 5, 823.
17. G. Catalan and J. F. Scott, *Adv. Mater*., **2009**, 21, 2463.
18. D. Lebeugle, D. Colson, A. Forget, M.Viret, P. Bonville, J. F. Marucco and S. Fusil, *Phys. Rev. B*, **2007**, 76, 024116.
19. T. Kimura, T. Goto, H. Shintani, K. Ishizaka, T. Arima and Y.Tokura, *Nature (London)*, **2003**, 426, 55.

20. T. Arima, D. Higashiyama, Y. Kaneko, J. P. He, T. Goto, S. Miyasaka, T. Kimura, K. Oikawa, T. Kamiyama, R. Kumai and Y. Tokura, *Phys. Rev. B*, **2004**,70, 064426.
21. P. Kumar, A. Bera, D. V. S. Muthu, S. N. Shirodkar, R. Saha, A. Shireen, A. Sundaresan, U. V. Waghmare, A. K. Sood and C. N. R. Rao, *Phys. Rev. B*, **2012**, 85, 134449.
22. S. Song, H. M. Jang, Nam-Suk Lee, J. Y. Son, R. Gupta, A. Garg, J. Ratanapreechachai and J. F. Scott, *NPG Asia Materials*, **2016**, 8, e242.
23. S. N. Achary, O. D. Jayakumar and A. K. Tyagi, *Elsevier Inc.* **2012**, pp. 155-191.
24. J. Laverdiere, S. Jandl, A. A. Mukhin, V. Y. Ivanov, V. G. Ivanov and M. N. Iliev, *Phys. Rev. B*, **2006**, 73, 214301.
25. M. O. Ramirez, A. Kumar, S. A. Denev, Y. H. Chu, J. Seidel, L. Martin, S. Y. Yang, R. C. Rai, X. Xue, J. F. Ihlefeld, N. J. Podraza, E. Saiz, S. Lee, J. Klug, S. W. Cheong, M. J. Bedzyk, O. Auciello, D. G. Schlom, J. Orenstein, R. Ramesh, J. L. Musfeldt, A. P. Litvinchuk and V. Gopalan, *Appl. Phys. Lett.*, **2009**, 94, 161905.
26. P. Kumar, S. Saha, D. V. S. Muthu, J. R. Sahu, A. K. Sood and C. N. R. Rao, *J. Phys.: Condens. Matter*, **2010**, 22, 115403.
27. M. Viswanathan, P. S. A. Kumar, V. S. Bhadram, C. Narayana, A. K. Bera and S. M. Yusuf, *J. Phys.: Condens. Matter*, **2010**, 22, 346006.
28. T. Nagai, D. Hamane, P. Sujatha Devi, N. Miyajima, T. Yagi, T. Yamanaka & K. Fujino, *J. Phys. Chem. B*, **2005**, 109, 39, 18226.
29. D. Errandonea, D. Santamaria-Perez, D. Martinez-Garcia, O. Gomis, R. Shukla, S. N. Achary, Avesh K. Tyagi & C. Popescu, *Inorg. Chem.*, **2017**, 56, 8363.
30. C. Toulouse, C. Martin, M-A. Measson, Y. Gallais, A. Sacuto and M. Cazayous, *Phys. Rev. B*, **2019**, 99, 024303.
31. S. Mukherjee, A. Garg and R. Gupta, *J. Phys.: Condens. Matter*, **2011**, 23, 445403.
32. J. F. Karpus, R. Gupta, H. Barath and S. L. Cooper, *Phys. Rev. Lett.*, **2004**, 93, 167205.
33. R. Saha, A. Shireen, A. K. Bera, S. N. Shirodkar, Y. Sundarayya, N. Kalarikkal, S. M. Yusuf, U. V. Waghmare, A. Sundaresan and C. N. R. Rao, *J. Solid State Chem.*, **2011**, 184, 494.
34. A. B. Sushkov, O. Tchernyshyov, W. Ratcliff, S. W. Cheong and H. D. Drew, *Phys. Rev. Lett.*, **2005**, 94, 137202.
35. M. Lang, J. M¨uller, F. Steglich, A. Br¨uhl, B. Wolf and M. Dressel, *J. Phys. IV (France)*, **2004**, 114, 111.
36. R. Shukla, K. Vasundhara, P. S. R. Krishna, A. B. Shinde, S. K. Sali, N. K. Kulkarni, S. N. Achary and A. K. Tyagi, *Int. J. Hydrogen Energy*, **2015**, 40, 15672.

37. Rodriguez-Carvajal J., *Multi Pattern Rietveld Refinement Program*: Fullprof 2000, July **2000** version 1.6.
38. K. N. Trueblood, H.-B. Bisirgi, H Burzlaff, J. D. Dunitz, C. M. Gramaccioli, H. H. Schulz, U. Shmueli & S. C. Abrahams, *Acta Cryst.*, **1996**, A52, 770.
39. J. Gonzalez-Platas, A. Munoz, P. Rodríguez-Hernandez & D. Errandonea, *Inorg. Chem.*, **2019**, 58, 5966.
40. M. K. Gupta, R. Mittal, M. Zbiri, R. Singh, S. Rols, H. Schober and S. L. Chaplot, *Phys. Rev. B,* **2014**, 90, 134304.
41. F. Bouree, J. L. Baudour, E. Elbadraoui, J. Musso, C. Laurent and A. Rousset, *Acta Cryst. B,* **1996**, 52, 217-222.
42. I. Urcelay-Olabarria, E. Ressouche, A. A. Mukhin, V. Yu. Ivanov, A. M. Balbashov, G. P. Vorobev, Yu. F. Popov, A. M. Kadomtseva, J. L. Garc´ıa-Munoz and V. Skumryev, *Phys. Rev. B,* **2012**, 85, 094436.
43. A. J. Campbell, G. Balakrishnan, M. R. Lees, D. McK. Paul and G. J. McIntyre, *Phys. Rev. B,* **1997**, 55, R8622.
44. S. Mukherjee, A. Garg and R. Gupta, *Appl. Phys. Lett.*, **2012**, 100, 112904.
45. W. M. Zhu and Z.-G. Ye, *Ceramics. Int*., **2004**, 30, 1435.
46. V. Singh, A. Daryapurkar, S. S. Rajput, S. Mukherjee, A. Garg and R. Gupta, *J. Am. Ceram. Soc.*, **2017**, 100, 5226.
47. X. Qi, J. Dho, R. Tomov, M. G. Blamire and J. L. MacManus-Driscoll, *Appl. Phys. Lett.*, **2005**, 86, 062903.
48. W. G. Fateley and F. R. Dollish, *Infrared and Raman Selection rules for Molecular and Lattice Vibrations*, Wiley-Interscience: New York, **1972**.
49. K. K. Mishra, V. Sivasubramanian and A. K. Arora, *J. Raman Spectrosc*., **2011**, 42, 517.
50. K. K. Mishra, A. T. Satya, A. Bharati, V. Sivasubramanian, V. R. K. Murthy and A. K. Arora, *J. Appl. Phys.*, **2011**, 110, 123529.
51. N. O. Golosova, D. P. Kozlenko, S. E. Kichanov, E. V. Lukin, L. S. Dubrovinsky, A. I. Mammadov, R. Z. Mehdiyeva, S. H. Jabarov, H. P. Liermann, K. V. Glazyrin, T. N. Dang, V. G. Smotrakov, V. V. Eremkin and B. N. Savenko, *J. Alloys Compd.*, **2016**, 684, 352.
52. B. A. Weinstein and R. Zallen, *Light Scattering in Solids IV, edited by M. Cardona and G. Guntherodt*; Springer-Verlag: Berlin, **1984**, pp.463.
53. E. Grando, A. Garc´ıa, J. A. Sanjurjo, C. Rettori, I. Torriani, F. Prado, R. D. S´anchez, A. Caneiro and S. B. Oseroff, *Phys. Rev. B*, **1999**, 60, 11879.

54. K. K. Mishra, S. Chandra, N. P. Salke, S. N. Achary, A. K. Tyagi and Rekha Rao, *Phys. Rev. B*, **2015**, 92, 134112.
55. R. Gupta, M. Kim, H. Barath, S. L. Cooper and G. Cao, *Phys. Rev. Lett.*, **2006**, 96, 1.
56. A. H. Morrish, *Physical Principles of Magnetism*; Wiley: New York, **1965**.
57. D. J. Lockwood and M. G. Cottam, *J. Appl. Phys.*, **1988**, 64, 5876.

Table captions

Table 1 Refined structural parameters for $Al_{0.5}Ga_{0.5}FeO_3$ as observed from PND data recorded at 300 K.

Table 2 Typical inter-atomic distances in $Al_{0.5}Ga_{0.5}FeO_3$ structure.

Table 3 Refined structural parameters for $Al_{0.5}Ga_{0.5}FeO_3$ as observed from PND data recorded at 7 K.

Table 4 Irreducible representations of different sites in the *Pc21n* unit cell of orthorhombic $Al_{0.5}Ga_{0.5}FeO_3$.

Table 5 Observed phonon mode frequencies observed at 82 and 300 K temperatures, and their mode assignments. The spin-phonon coupling constants, λ estimated for several phonon modes are also presented.

Figure captions

Fig. 1(a) Rietveld refinement plot of the powder neutron diffraction data recorded at 300 K, and (b) crystallographic orthorhombic structure (*Pc2₁n*) of $Al_{0.5}Ga_{0.5}FeO_3$ at ambient conditions.

Fig. 2 Temperature evolution of powder neutron diffraction pattern. Arrow marks indicate the magnetic reflections (110) and (020) located at 11.2° and 15.3°, respectively in the diffraction pattern.

Fig. 3(a) Rietveld refinement plot of the powder neutron diffraction data recorded at 7 K. Vertical ticks Bragg positions for chemical (upper row) and magnetic (lower row) structures. (Orthorhombic: *Pc2₁n* , a = 8.635(2) Å, b = 9.315(1) Å, c = 5.022(1) Å, V = 403.9(1) Å^3; Rp: 5.94, Rwp: 8.19, Chi2: 11.0, R_{Bragg}: 6.09, R_F: 3.65; Magnetic R_B: 11.1). (b) Rietveld refinement plot of the powder neutron diffraction data recorded at 773 K. Vertical ticks show Bragg positions for chemical structures (Orthorhombic: *Pc2₁n*, *a* = 8.6746(6) Å, *b* = 9.3627(5) Å, *c* = 5.0502(3) Å, *V* = 410.16(5) Å^3; Rp: 4.82 Rwp: 6.36, Chi2: 6.10, R_{Bragg}: 4.82, R_F = 3.54).

Fig. 4 Magnetic structure of $Al_{0.5}Ga_{0.5}FeO_3$ (the site moments are shown by vectors; M1, M2, M3 and M4 are defined in Table 1).

Fig. 5 Thermal evolution of integrated intensity ($I_{(T)}/I_{7K} \times 100$, where $I_{(T)}$ and I_{7K} are integrated intensity of the peaks at temperature T and 7 K) of the magnetic reflections (110) and (020) located at 2θ positions 11.2°and 15.3°, respectively indicating the change of magnetic ordering above 225 K.

Fig. 6 Evolution of unit cell parameters and volume of unit cell of ALGF with temperature.

Fig.7(a) FC and ZFC magnetization curves of ALGF at static applied magnetic field of 1 kOe, and (b) *M-H* hysteresis loops at different temperatures (3-300 K). Inset: shows incomplete paramagnetic phase at 300 K.

Fig. 8 Raman spectrum observed at ambient temperature fitted to sum of Lorentzian peaks in the frequency ranges (a) 200-1000 cm^{-1} and (b) 1000-1900 cm^{-1}. Solid curves are the Lorentzian least-square fits to data. Individual fitted peaks are also shown.

Fig. 9 Raman spectra of ALGF at different temperatures measured in the frequency range 200-1000 cm^{-1}. Solid curves are the Lorentzian least-square fits to data. Raman spectrum measured at 82 K, fitted to a sum of 12 Lorentzian peaks are individually shown.

Fig. 10(a) Raman spectra of ALGF measured at different temperatures in the frequency range 1000-1900 cm^{-1}. Solid curves are the Lorentzian least-square fits to data, (b) Temperature dependence of second order mode frequencies. Straight lines through the data are linear least square fit to the data. Mode at 1272 cm^{-1} originated from two-magnon phonon scattering processes.

Fig. 11 Dependencies of mode frequencies on temperature for several characteristic phonons. The anharmonicity model was used to analyzed the data in the paramagnetic phase above 240 K. Extrapolated phonon mode positions in the ferrimagnetic phase below 240 K were used to extract the frequency shifts ($\Delta\omega$), and are attributed to spin-phonon coupling contributions.

Fig. 12 Plots of $\omega(T)$ versus $[M(T)/Ms]^2$ are shown for 270, 425, 582, 695, 738 and 831 cm^{-1} modes. Linear least square fits to the data are shown by solid lines. Slope of these lines essentially represents spin-phonon coupling constants, λ.

Table 1. Refined structural parameters for $Al_{0.5}Ga_{0.5}FeO_3$ as obtained from PND data recorded at 300 K.

Name		Site	x	y	z	B	occ
M1	Ga1t	*4a*	0.1560(5)	0	0.1732(8)	0.69(7)	0.43(1)
	Al1t	*4a*	0.1560(5)	0	0.1732(8)	0.69(7)	0.36(2)
	Fe1t	*4a*	0.1560(5)	0	0.1732(8)	0.69(7)	0.21(1)
M2	Ga2	*4a*	0.1584(4)	0.3091(4)	0.8144(6)	0.41(9)	0.38(1)
	Al2	*4a*	0.1584(4)	0.3091(4)	0.8144(6)	0.41(9)	0.44(2)
	Fe2	*4a*	0.1584(4)	0.3091(4)	0.8144(6)	0.41(9)	0.21(1)
M3	Fe3	*4a*	0.1525(3)	0.5825(3)	0.1920(6)	0.28(8)	0.89(1)
	Al3	*4a*	0.1525(3)	0.5825(3)	0.1920(6)	0.28(8)	0.12(2)
	Ga3	*4a*	0.1525(3)	0.5825(3)	0.1920(6)	0.28(8)	0.02(0)
M4	Fe4	*4a*	0.0321(3)	0.7976(3)	0.6779(6)	0.57(9)	0.67(1)
	Al4	*4a*	0.0321(3)	0.7976(3)	0.6779(6)	0.57(9)	0.14(2)
	Ga4	*4a*	0.0321(3)	0.7976(3)	0.6779(6)	0.57(9)	0.20(1)
O1		*4a*	0.3226(4)	0.4254(4)	0.9779(7)	0.5(1)	1
O2		*4a*	0.4900(4)	0.4350(5)	0.5145(8)	0.9(2)	1
O3		*4a*	0.9988(7)	0.2008(6)	0.6537(10)	0.5(1)	1
O4		*4a*	0.1588(5)	0.1978(4)	0.1572(9)	0.5(1)	1
O5		*4a*	0.1666(7)	0.6713(7)	0.8498(10)	0.8(1)	1
O6		*4a*	0.1660(8)	0.9397(10)	0.5086(11)	0.7(1)	1

Orthorhombic, $Pc2_1n$
a = 8.6437(5) Å, b = 9.3230(4) Å, c = 5.0283(3) Å, V = 405.20(4) Å^3
Rp: 5.01, Rwp: 6.70, Chi2: 6.87, R_{Bragg}: 4.02, R_F: 3.04

Table 2 Typical inter-atomic distances (Å) in $Al_{0.5}Ga_{0.5}FeO_3$ structure.

M1 (tetra)	Distance (Å)	M2(octa.)	Distance (Å)	M2(octa.)	Distance (Å)	M4(octa.)	Distance (Å)
M1-O2	1.821(6)	M2-O1	1.966(5)	M3-O1	2.338(5)	M4-O1	2.305(5)
M1-O4	1.846(4)	M2-O1	2.016(5)	M3-O1	2.064(5)	M4-O2	2.041(5)
M1-O6	1.780(7)	M2-O2	2.009(5)	M3-O2	2.051(5)	M4-O3	1.915(6)
M1-O6	1.835(8)	M2-O3	1.891(7)	M3-O3	1.879(6)	M4-O4	2.068(5)
		M2-O4	2.012(5)	M3-O5	1.913(6)	M4-O5	1.867(7)
		M2-O4	2.045(6)	M3-O5	1.939(7)	M4-O6	1.954(8)
Average	1.821(3)		1.991(2)		2.031(2)		2.025(3)
CN:	4		6		6		6
Dist.	1.904×10^{-4}		6.474×10^{-4}		57.079×10^{-4}		49.840×10^{-4}

(M: $Ga^{3+}/Al^{3+}/Fe^{3+}$ as given in Table 1)

Table 3. Refined structural parameters for $Al_{0.5}Ga_{0.5}FeO_3$ as obtained from PND data recorded at 7 K.

Name	Atoms	Site	x	y	z	occ	Moment (μ_B)
M1	Ga1t	*4a*	0.1552(5)	0.0003(4)	0.1831(8)	0.43	
	Al1t	*4a*				0.36	
	Fe1t	*4a*				0.21	-3.775
M2	Ga2	*4a*	0.1569(4)	0.3095(4)	0.8101(6)	0.38	
	Al2	*4a*				0.44	
	Fe2	*4a*				0.21	4.575
M3	Fe3	*4a*	0.1511(4)	0.5831(3)	0.1885(6)	0.89	-3.775
	Al3	*4a*				0.12	
	Ga3	*4a*				0.02	
M4	Fe4	*4a*	0.0304(3)	0.7978(3)	0.6822(6)	0.67	4.375
	Al4	*4a*				0.14	
	Ga4	*4a*				0.20	
	O1	*4a*	0.3216(4)	0.4269(4)	0.9755(7)	1	
	O2	*4a*	0.4913(5)	0.4362(5)	0.5089((8)	1	
	O3	*4a*	0.9979(8)	0.2007(8)	0.6495(10)	1	
	O4	*4a*	0.1612(5)	0.1973(4)	0.1526(9)	1	
	O5	*4a*	0.1647(7)	0.6669(8)	0.8405(11)	1	
	O6	*4a*	0.1667(9)	0.9397(11)	0.5189(8)	1	

Orthorhombic, *$Pc2_1n$;* $B_{ov.}$ = 0.19 $Å^2$
a = 8.635(2) Å, b = 9.315(1) Å, c = 5.022(1) Å, V = 403.9(1) $Å^3$
Rp: 5.94, Rwp: 8.19, Chi2: 11.0, R_{Bragg}: 6.09, R_F: 3.65; Magnetic R_B: 11.1
Magnetic moment = 0.13 μ_B/Fe^{3+}

Table 4 Irreducible representations of different sites in the *Pc2₁n* unit cell of orthorhombic $Al_{0.5}Ga_{0.5}FeO_3$.

Atom[a]	Site	Irreducible representation
M1	4a(C_1)	$3A_1+3A_2+3B_1+3B_2$
M2	4a(C_1)	$3A_1+3A_2+3B_1+3B_2$
M3	4a(C_1)	$3A_1+3A_2+3B_1+3B_2$
M4	4a(C_1)	$3A_1+3A_2+3B_1+3B_2$
O	4a(C_1)	$18A_1+18A_2+18B_1+18B_2$
		$\Gamma_{total} = 30\ A_1+ 30\ A_2+ 30B_1+ 30B_2$
		$\Gamma_{Raman}= 29\ A_1+ 30\ A_2+ 29\ B_1+29\ B_2$
		$\Gamma_{IR}= 29\ A_1+ 29\ B_1+ 29\ B_2$

[a](M: $Ga^{3+}/Al^{3+}/Fe^{3+}$ as given in Table 1)

Table 5 Observed mode frequencies of $Al_{0.5}Ga_{0.5}FeO_3$ measured at 82 and 300 K, and their mode assignments.[a] The spin-phonon coupling constants, λ for several phonon modes are also included.

Mode frequency (cm^{-1})		Mode description	Spin-phonon coupling constant, λ
82 K	**298 K**		
270	263		2.3
324	322	Libration mode of polyhedral units	
376	372		
426	419	Bending mode vibration of polyhedral units	1.15
491	496		
582	578		1.35
652	642	Stretching mode vibration of polyhedral units	
696	691		0.5
739	736		0.55
841	838		1.1
912	907		
1271	-	Two-magnon band	
1452	1448	Overtone	
1566	1559	Combination band	
1679	1661	Overtone	

[a]Ref. 51

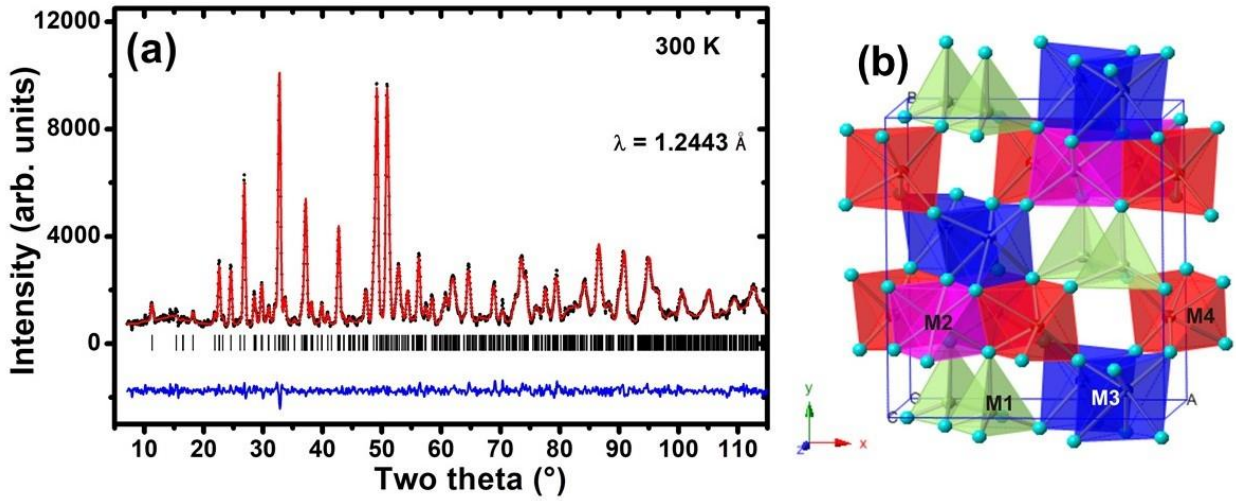

Fig. 1(a) Rietveld refinement plot of the powder neutron diffraction data recorded at 300 K, and (b) crystallographic orthorhombic structure (*Pc2₁n*) of $Al_{0.5}Ga_{0.5}FeO_3$ at ambient conditions.

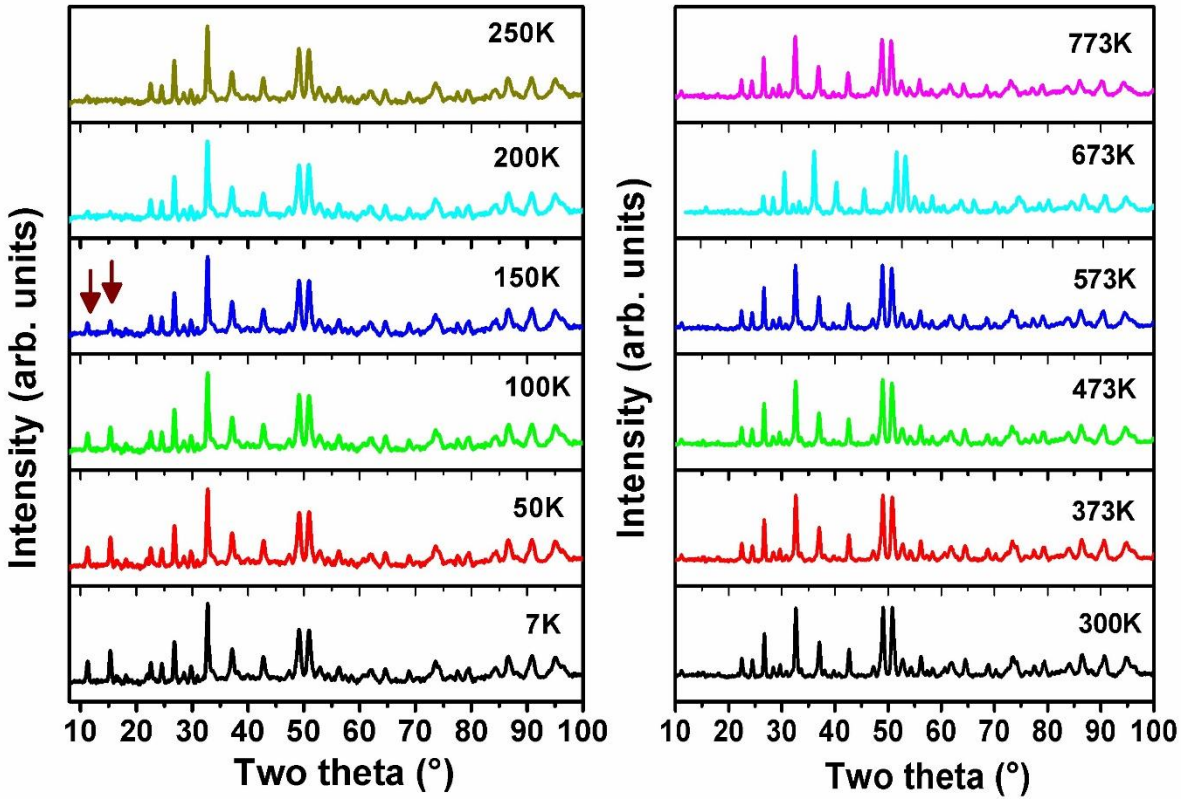

Fig. 2 Temperature evolution of powder neutron diffraction pattern. Arrow marks indicate the magnetic reflection (110) and (020) located at 11.2^{o} and 15.3^{o}, respectively in the diffraction pattern.

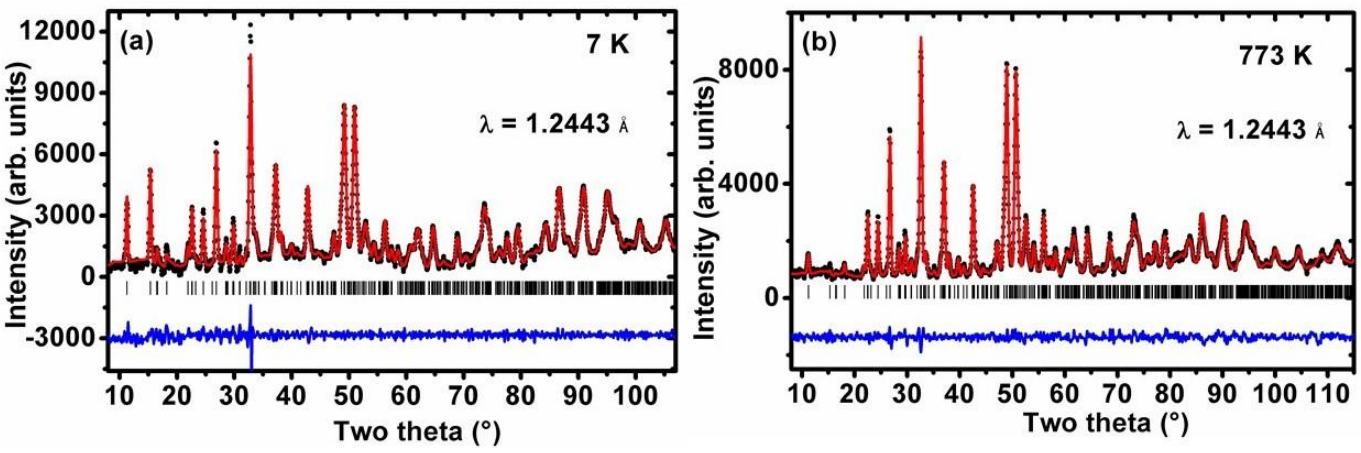

Fig. 3(a) Rietveld refinement plot of the powder neutron diffraction data recorded at 7 K. Vertical ticks Bragg positions for chemical (upper row) and magnetic (lower row) structures. (Orthorhombic: $Pc2_1n$, a = 8.635(2) Å, b = 9.315(1) Å, c = 5.022(1) Å, V = 403.9(1) Å^3; Rp: 5.94, Rwp: 8.19, Chi2: 11.0, R_{Bragg}: 6.09, R_F: 3.65; Magnetic R_B: 11.1), (b) Rietveld refinement plot of the powder neutron diffraction data recorded at 773 K. Vertical ticks show Bragg positions for chemical structures (Orthorhombic: $Pc2_1n$, a = 8.6746(6) Å, b = 9.3627(5) Å, c = 5.0502(3) Å, V = 410.16(5) Å^3; Rp: 4.82 Rwp: 6.36, Chi2: 6.10, R_{Bragg}: 4.82, R_F = 3.54).

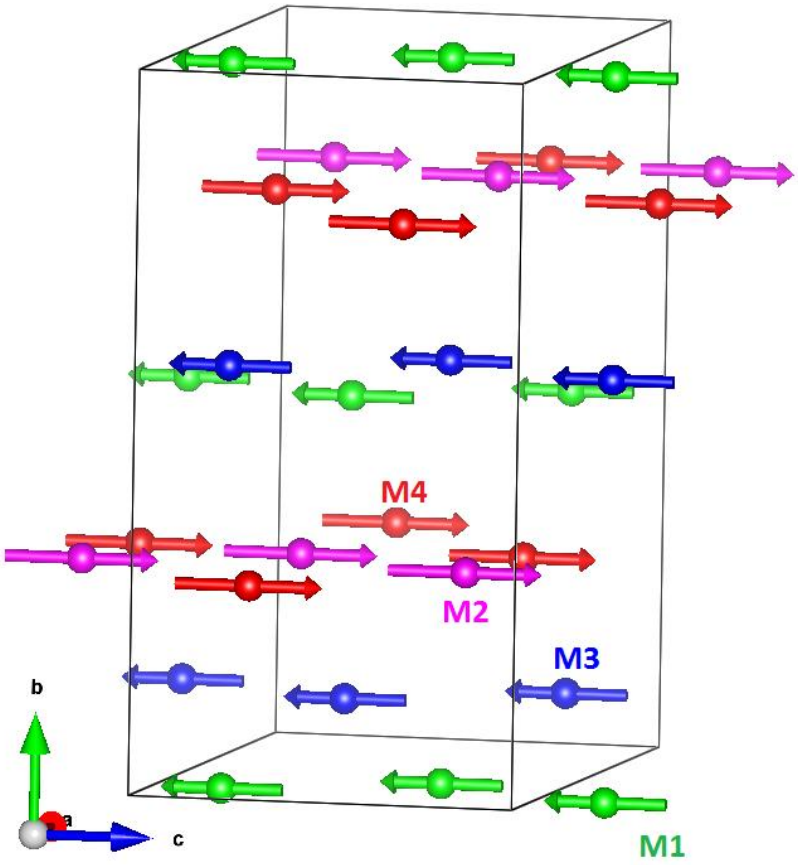

Fig. 4 Magnetic structure of $Al_{0.5}Ga_{0.5}FeO_3$ (the site moments are shown by vectors; M1, M2, M3 and M4 are defined in Table 1).

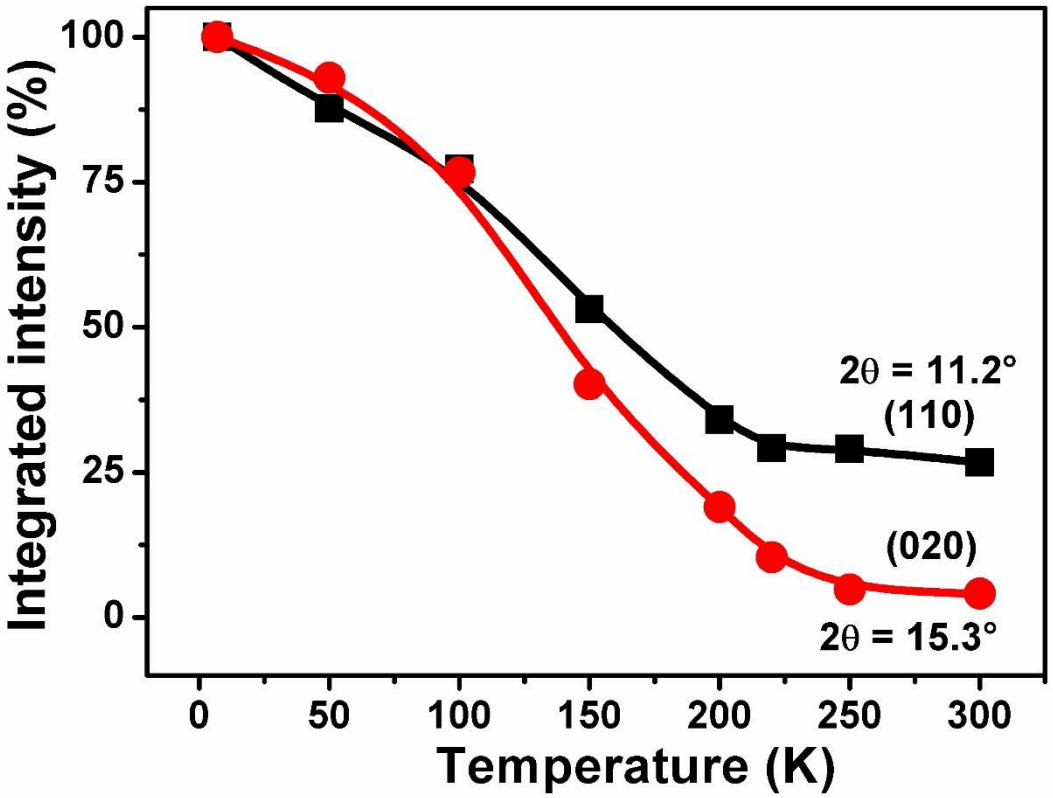

Fig. 5 Thermal evolution of integrated intensity ($I_{(T)}/I_{7K} \times 100$, where $I_{(T)}$ and I_{7K} are integrated intensity of the peaks at temperature T and 7 K) of the magnetic reflection (110) and (020) located at 2θ positions 11.2° and 15.3°, respectively indicating the change of magnetic ordering above 225 K.

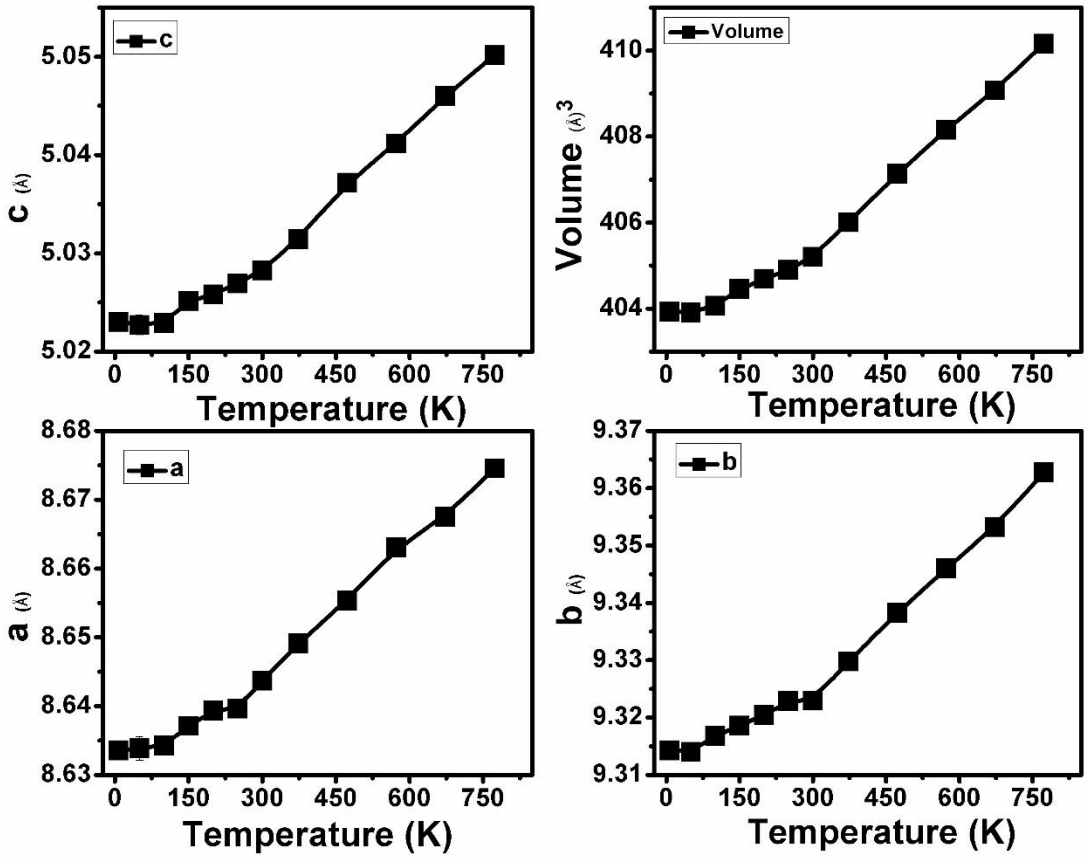

Fig. 6 Evolution of unit cell parameters and volume of unit cell of ALGF with temperature.

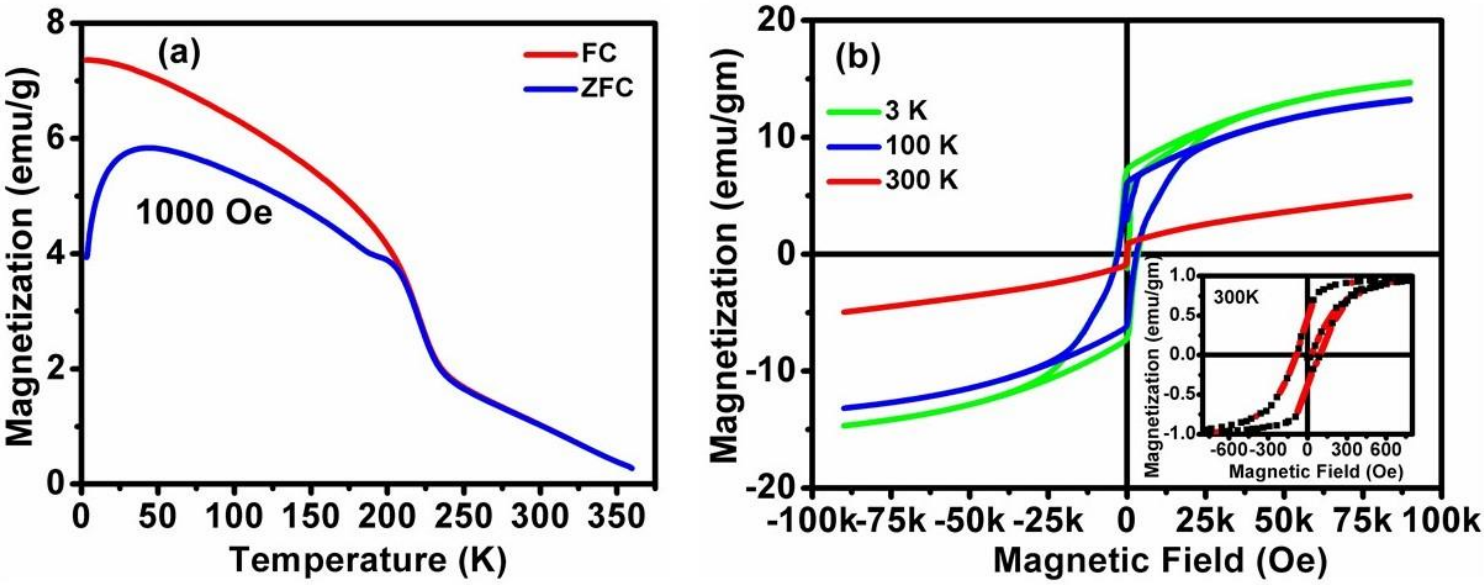

Fig. 7(a) FC and ZFC magnetization curves of ALGF at static applied magnetic field of 1 kOe, and (b) *M-H* hysteresis loops at different temperatures (3-300 K). Inset: shows incomplete paramagnetic phase at 300 K.

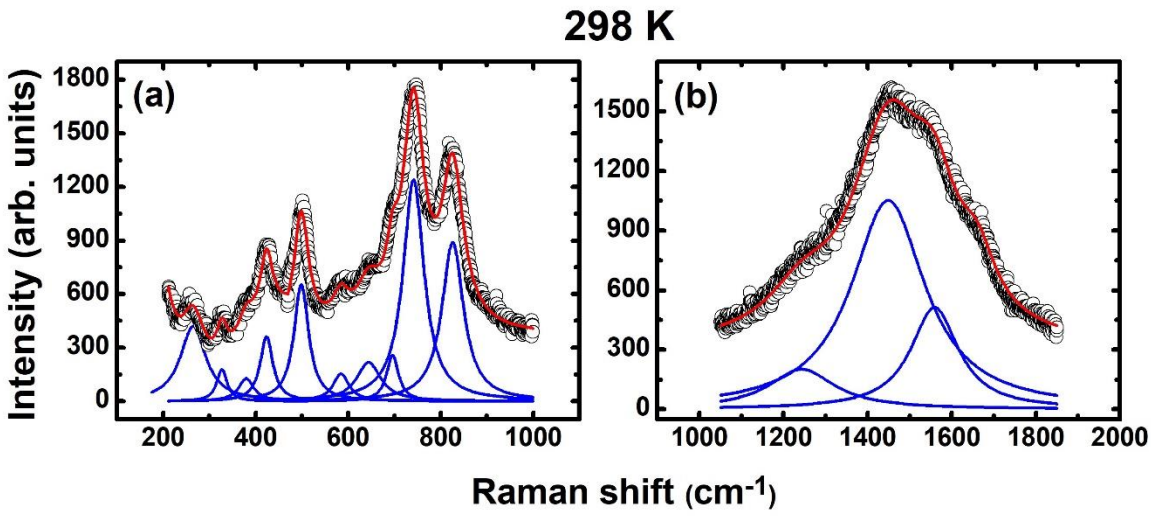

Fig. 8 Raman spectrum observed at ambient temperature fitted to a sum of Lorentzian peaks in the frequency range (a) 200- 1000 cm^{-1} and (b) 1000-1900 cm^{-1}. Solid curves are the Lorentzian least-square fits to data. Individual fitted peaks are also shown.

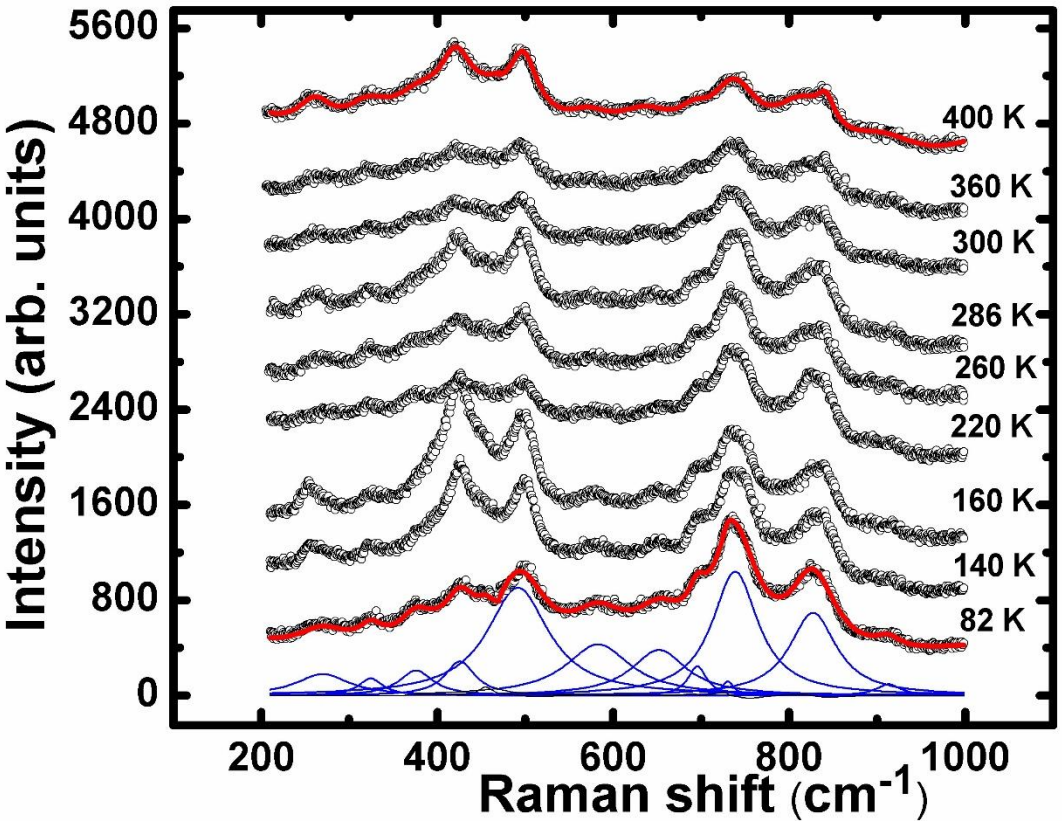

Fig. 9 Raman spectra of ALGF at different temperatures measured in the frequency range 200-1000 cm^{-1}. Solid curves are the Lorentzian least-square fits to data. Raman spectrum measured at 82 K, fitted to a sum of 12 Lorentzian peaks are individually shown.

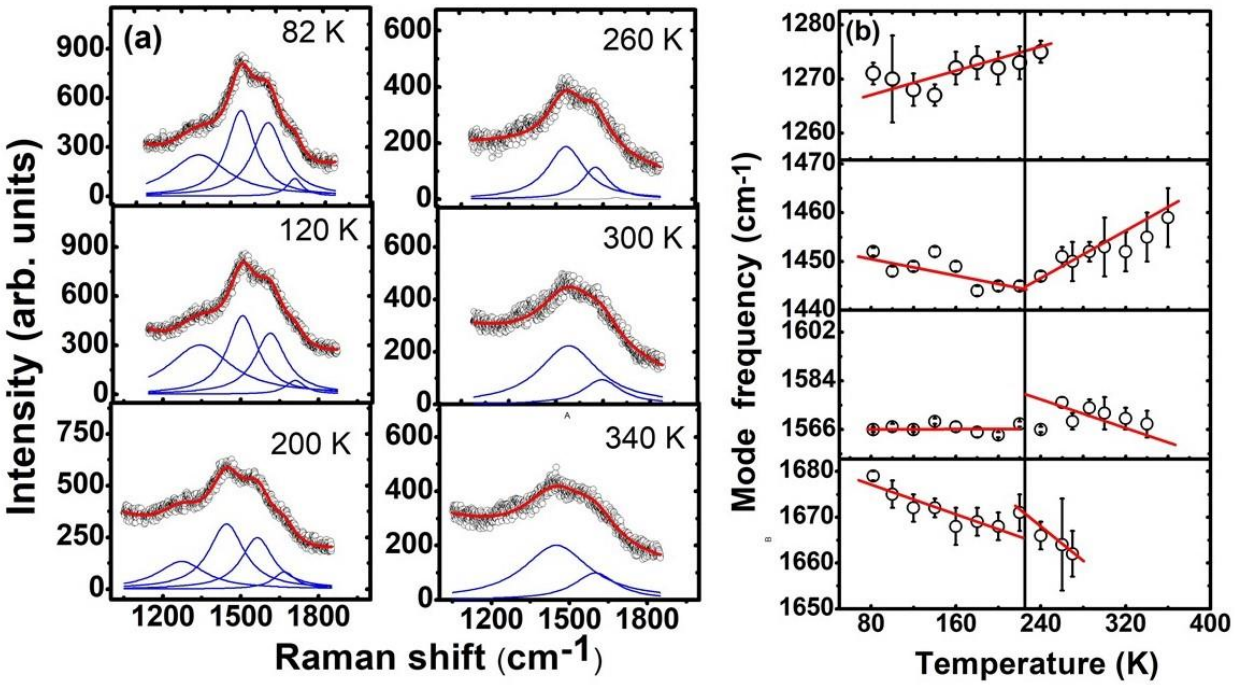

Fig. 10 (a) Raman spectra of ALGF measured at different temperatures in the frequency range 1000-1900 cm^{-1}. Solid curves are the Lorentzian least-square fits to data, (b) Temperature dependence of second order mode frequencies. Straight lines through the data are linear least square fit to the data. Mode at 1272 cm^{-1} originated from two-magnon phonon scattering processes.

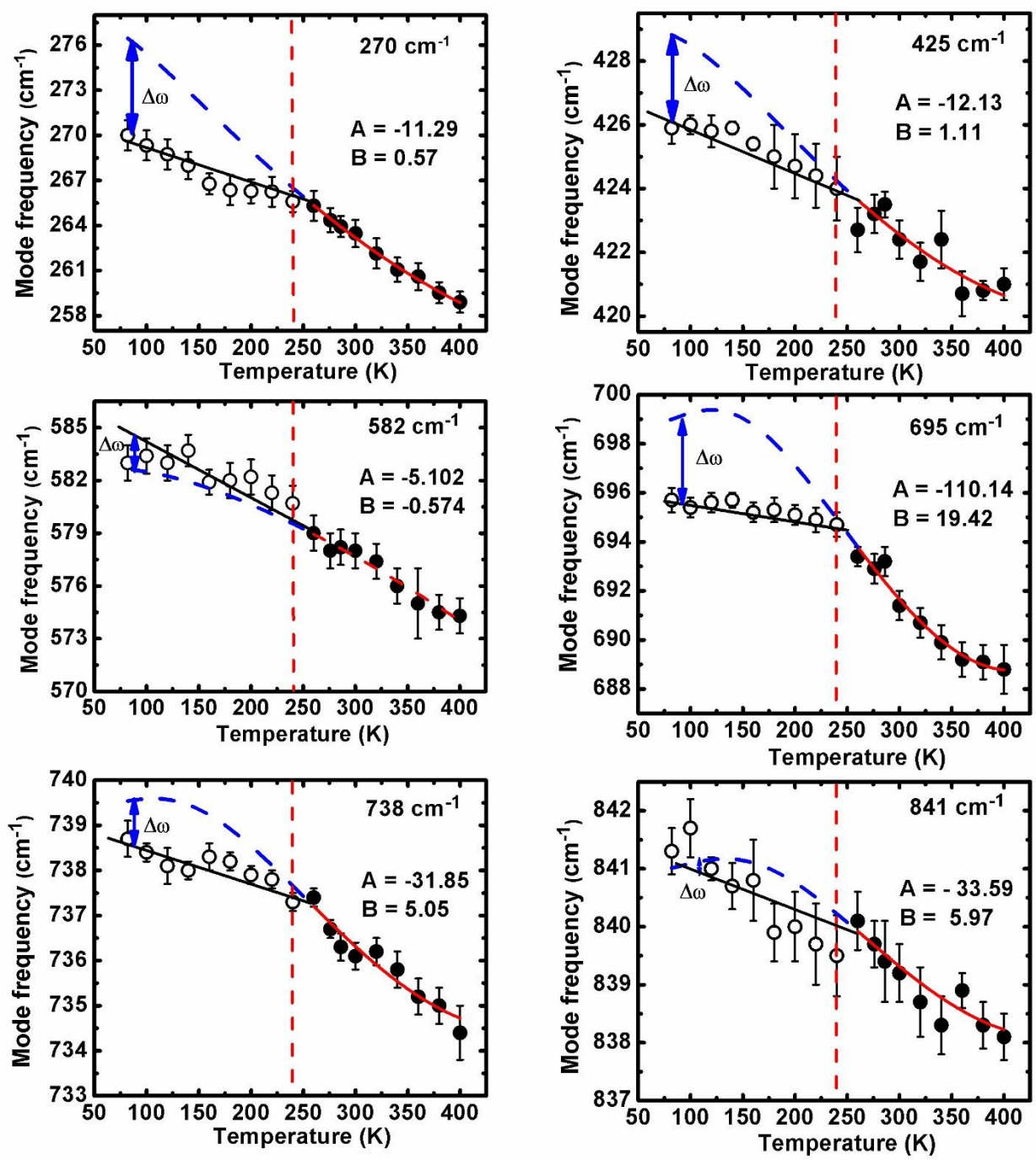

Fig. 11 Dependencies of mode frequencies on temperature for several characteristic phonons. The anharmonicity model was used to analyzed the data in the paramagnetic phase above 240 K. Extrapolated phonon mode positions in the ferrimagnetic phase below 240 K were used to extract the frequency shifts (Δω), and are attributed to spin-phonon coupling contribution.

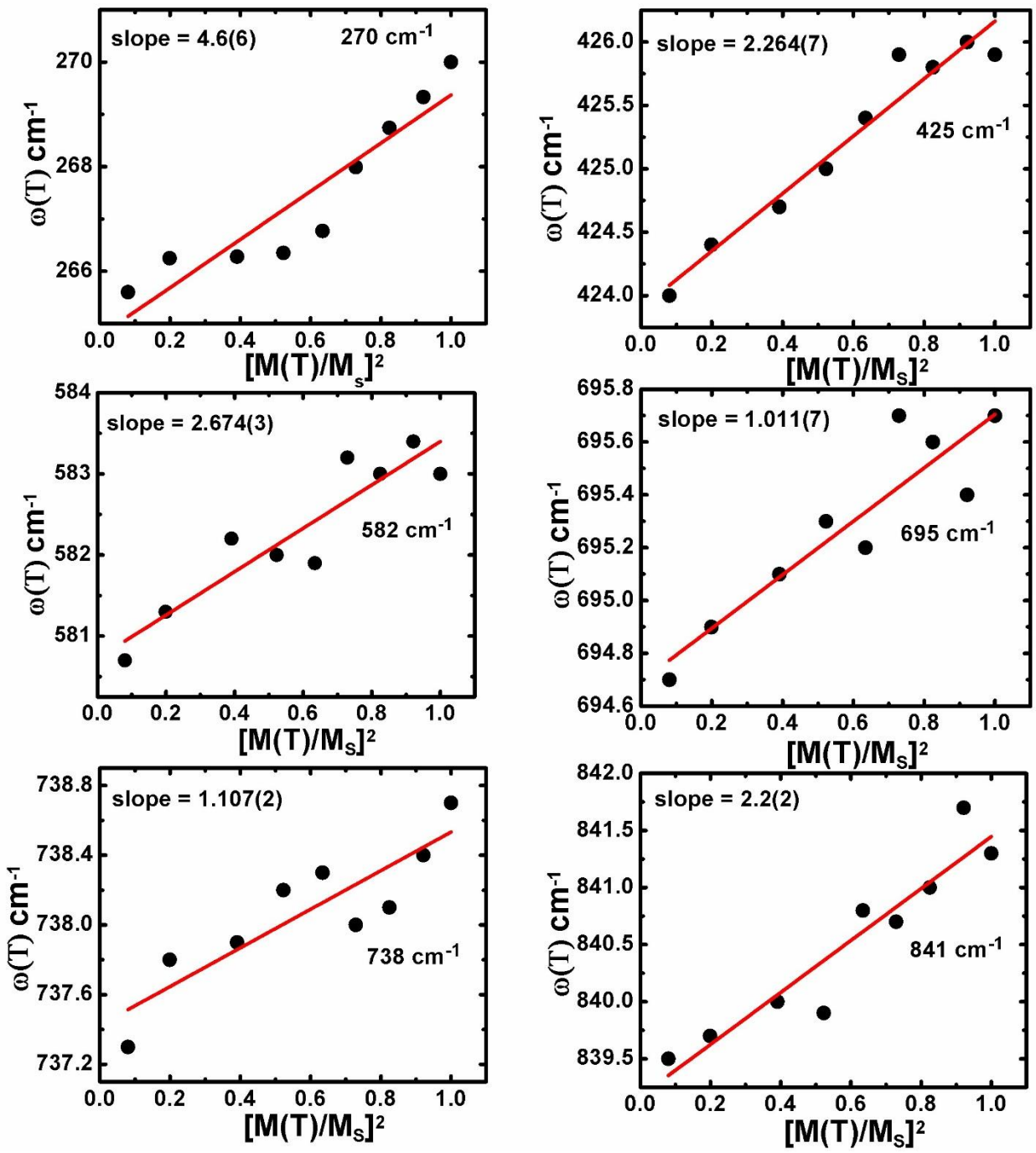

Fig. 12 Plots of ω(T) versus $[M(T)/Ms]^2$ are shown for 270, 425, 582, 695, 738 and 841 cm^{-1} modes. Linear least square fits to the data are shown by solid lines. Slopes of these lines essentially represent spin-phonon coupling constants, λ.

Table of Contents:

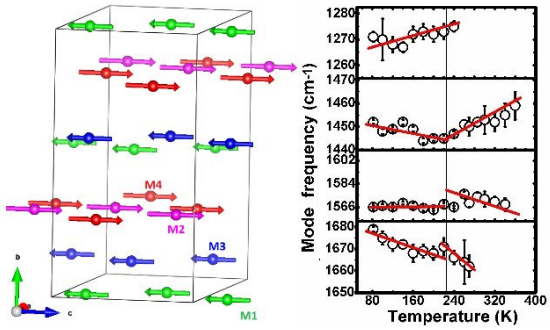

Magnetoelastic behaviour in $Al_{0.5}Ga_{0.5}FeO_3$ have been investigated using variable temperature neutron diffraction and Raman spectroscopy.